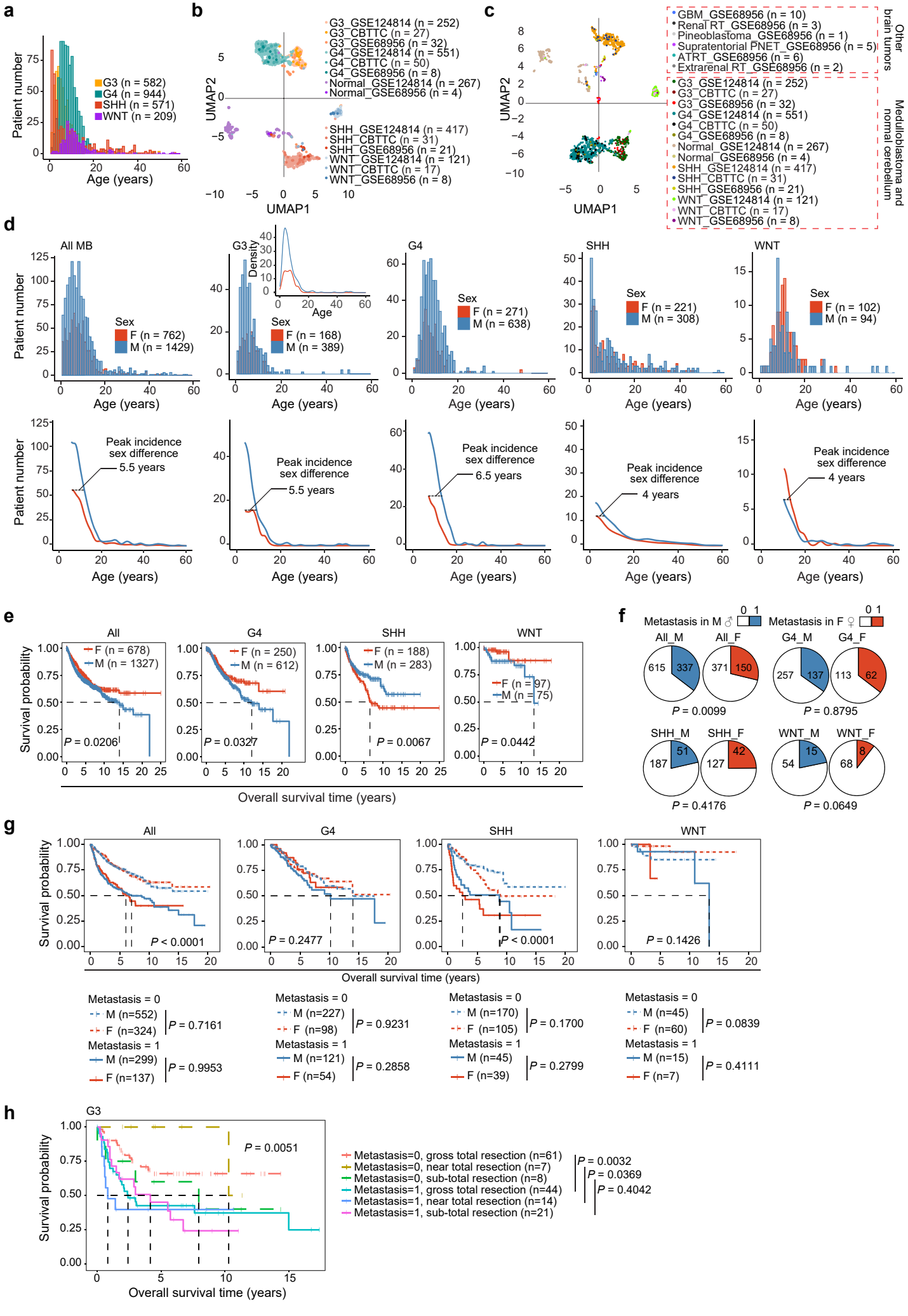
a
Patient number
Age (years)
G3 (n = 582)
G4 (n = 944)
SHH (n = 571)
WNT (n = 209)
b
UMAP1
UMAP2
G3_GSE124814 (n = 252)
G3_CBTTC (n = 27)
G3_GSE68956 (n = 32)
G4_GSE124814 (n = 551)
G4_CBTTC (n = 50)
G4_GSE68956 (n = 8)
Normal_GSE124814 (n = 267)
Normal_GSE68956 (n = 4)
SHH_GSE124814 (n = 417)
SHH_CBTTC (n = 31)
SHH_GSE68956 (n = 21)
WNT_GSE124814 (n = 121)
WNT_CBTTC (n = 17)
WNT_GSE68956 (n = 8)
c
GBM_GSE68956 (n = 10)
Renal RT_GSE68956 (n = 3)
Pineoblastoma_GSE68956 (n = 1)
Supratentorial PNET_GSE68956 (n = 5)
ATRT_GSE68956 (n = 6)
Extrarenal RT_GSE68956 (n = 2)
Other brain tumors
Medulloblastoma and normal cerebellum
d
All MB
Sex
F (n = 762)
M (n = 1429)
G3
Density
F (n = 168)
M (n = 389)
G4
F (n = 271)
M (n = 638)
SHH
F (n = 221)
M (n = 308)
WNT
F (n = 102)
M (n = 94)
Peak incidence sex difference
5.5 years
5.5 years
6.5 years
4 years
4 years
e
All
G4
SHH
WNT
Survival probability
F (n = 678)
M (n = 1327)
P = 0.0206
F (n = 250)
M (n = 612)
P = 0.0327
F (n = 188)
M (n = 283)
P = 0.0067
F (n = 97)
M (n = 75)
P = 0.0442
Overall survival time (years)
f
Metastasis in M ♂
Metastasis in F ♀
All_M
All_F
G4_M
G4_F
615
337
371
150
257
137
113
62
P = 0.0099
P = 0.8795
SHH_M
SHH_F
WNT_M
WNT_F
187
51
127
42
54
15
68
8
P = 0.4176
P = 0.0649
g
All
G4
SHH
WNT
Survival probability
P < 0.0001
P = 0.2477
P < 0.0001
P = 0.1426
Overall survival time (years)
Metastasis = 0
M (n=552)
F (n=324)
P = 0.7161
Metastasis = 1
M (n=299)
F (n=137)
P = 0.9953
Metastasis = 0
M (n=227)
F (n=98)
P = 0.9231
Metastasis = 1
M (n=121)
F (n=54)
P = 0.2858
Metastasis = 0
M (n=170)
F (n=105)
P = 0.1700
Metastasis = 1
M (n=45)
F (n=39)
P = 0.2799
Metastasis = 0
M (n=45)
F (n=60)
P = 0.0839
Metastasis = 1
M (n=15)
F (n=7)
P = 0.4111
h
G3
Survival probability
P = 0.0051
Overall survival time (years)
Metastasis=0, gross total resection (n=61)
Metastasis=0, near total resection (n=7)
Metastasis=0, sub-total resection (n=8)
Metastasis=1, gross total resection (n=44)
Metastasis=1, near total resection (n=14)
Metastasis=1, sub-total resection (n=21)
P = 0.0032
P = 0.0369
P = 0.4042

Extended Data Fig. 1 Incidence and prognosis across MB subgroups. a, Histogram depicting the incidence of different MB subgroups along with age. **b**, UMAP visualization of bulk RNA-seq data from various MB subgroups and studies. **c**, UMAP visualization of bulk RNA-seq data from different brain tumor types and studies. **d**, Histogram showing sex-specific incidence trends across MB subgroups and age groups. **e**, Kaplan-Meier survival curve comparing sexes within each MB subgroup. **f**, Pie charts illustrating sex differences in metastasis incidence of MB subgroups. **g**, Kaplan-Meier survival curve analyzing survival stratified by sex and metastasis status in each MB. subgroup. **h**, Kaplan-Meier survival curve for G3 MB patients stratified by metastasis status and extent of surgical resection. Each dot represents one bulk RNA-seq sample (**b, c**). *n* denotes the number of human samples analyzed (**a–e, g, h**). *P* values were calculated using the log-rank test (**e, g, h**) or chi-square test (**f**).

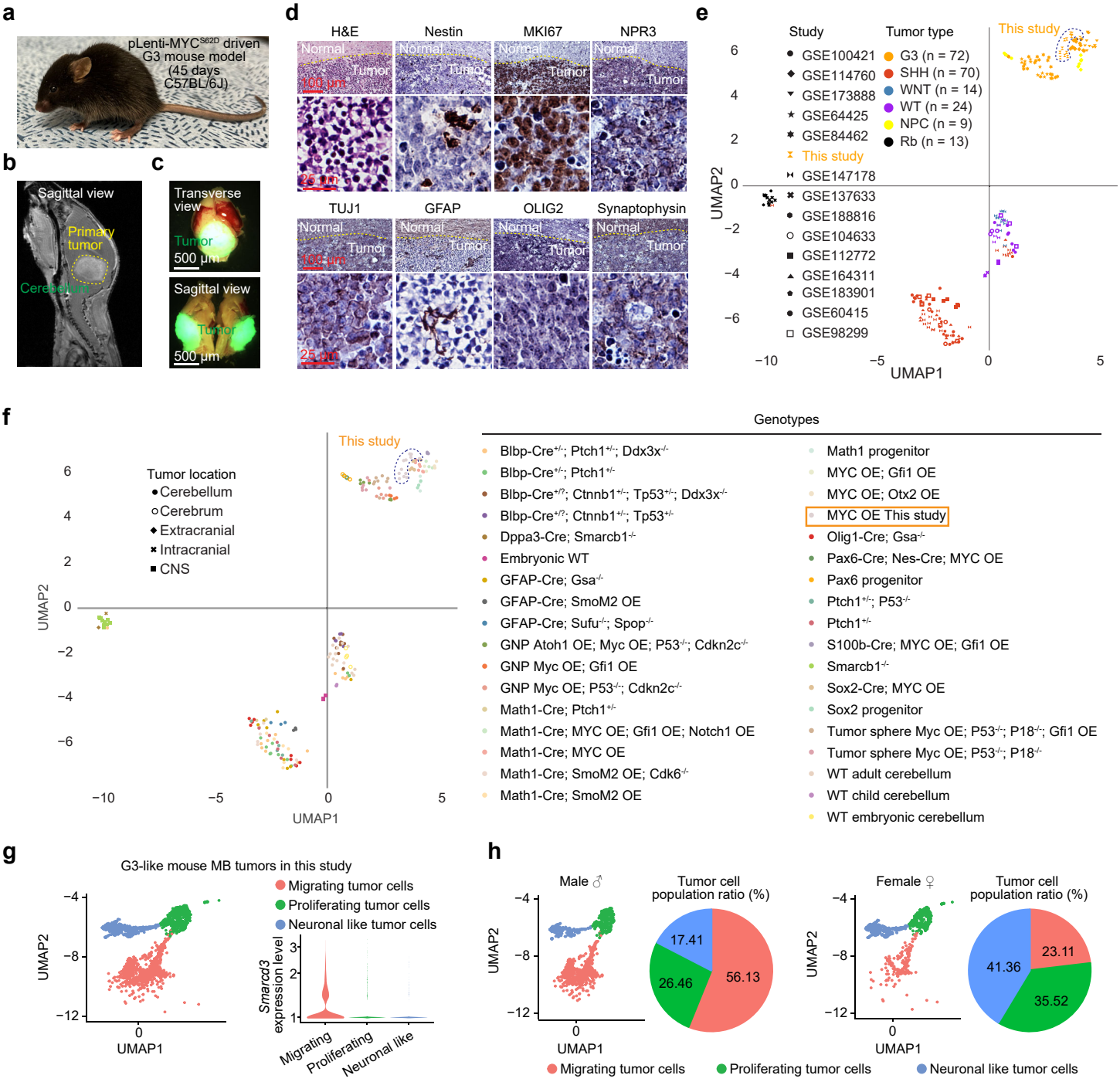

Extended Data Fig. 2 Characterization of the G3-like mouse model. a, Image of a C57BL/6J mouse with a cerebellar G3-like tumor induced by pLenti-MYC^{S62D}. **b**, MRI showing the cerebellar tumor. **c**, Bright-field and fluorescence images of tumor-bearing mouse brains. **d**, H&E and IHC staining of pLenti-MYC^{S62D}-induced tumors for the indicated marker genes. **e**, UMAP visualization of the mouse bulk RNA-seq data from different subgroups and studies. **f**, UMAP visualization of transgenic mouse brain tumors or mouse cells from the bulk RNA-seq data. **g**, UMAP visualization of tumor cells from pLenti-MYC^{S62D}-induced G3-like mouse tumors and violin plot showing SMARCD3 mRNA expression levels in the indicated tumor cell groups. **h**, UMAP visualization of pLenti-MYC^{S62D}-induced G3-like tumor cell populations, and pie charts illustrating the component ratio of tumor cell groups in sexes. *n* represents the number of mouse samples (**e**).

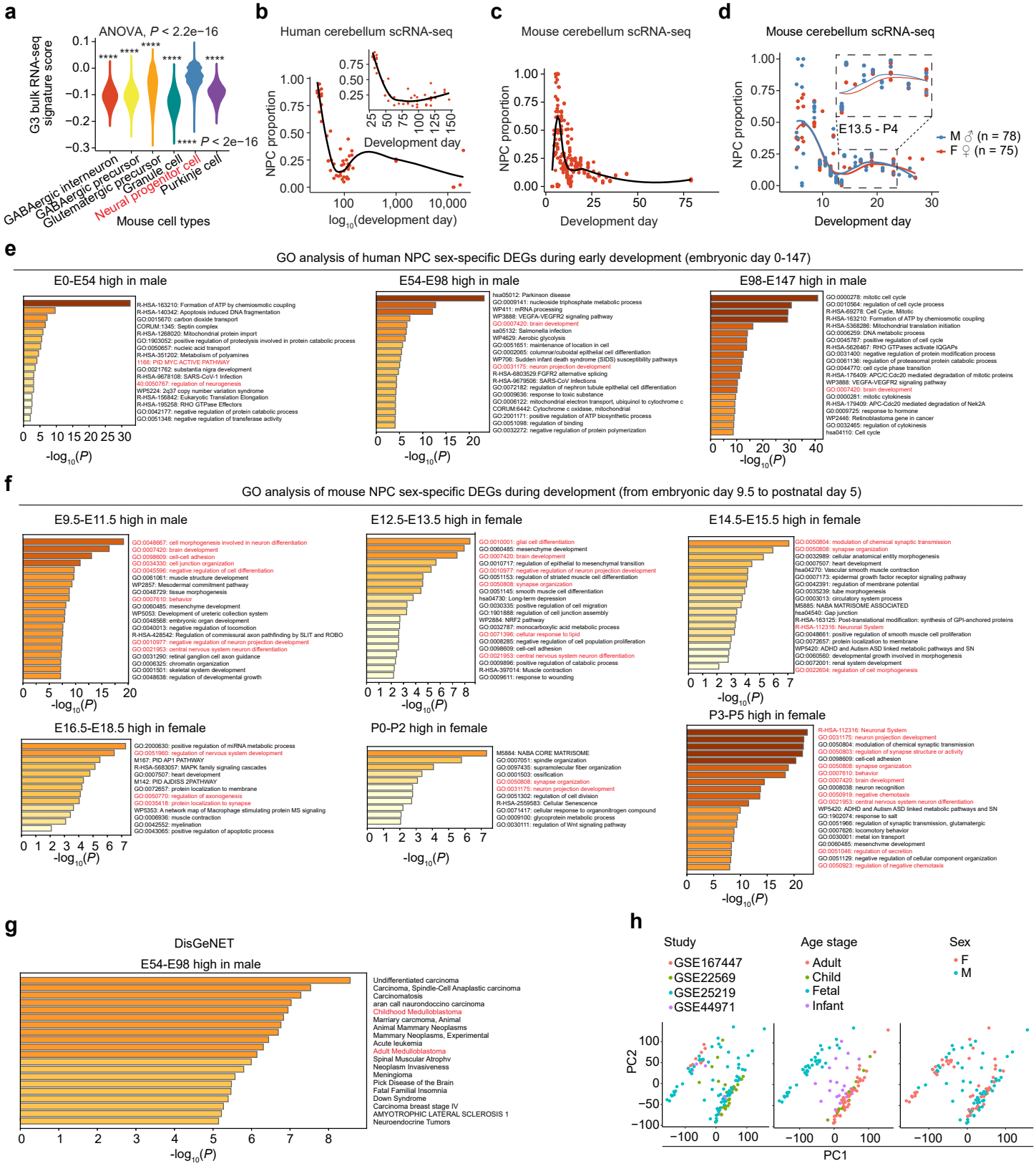

Extended Data Fig. 3 Sexual dimorphic properties of cerebellar NPCs. a, Violin plot of G3 bulk RNA-seq signature scores across cerebellar cell types. **b–d**, scRNA-seq data analyses of NPC proportions in human (**b**) and mouse (**c, d**) cerebellum during development. **e–f**, GO analyses of sex-specific DEGs in human (**e**) and mouse (**f**) NPCs. **g**, Diseases enrichment analysis in sex-specific DEGs of human NPC. **h**, PCA of human bulk RNA-seq data across studies, age groups, and sexes. Each dot represents a merged sample from scRNA-seq data (**b–d**) or a bulk RNA-seq sample (**h**). *n* denotes the number of mouse samples (**d**). *P* values were calculated using one-way ANOVA (**a**), two-tailed Welch's *t*-test with FDR correction (**a**), or two-tailed Benjamini-Hochberg corrected multiple Fisher test (**e–g**).

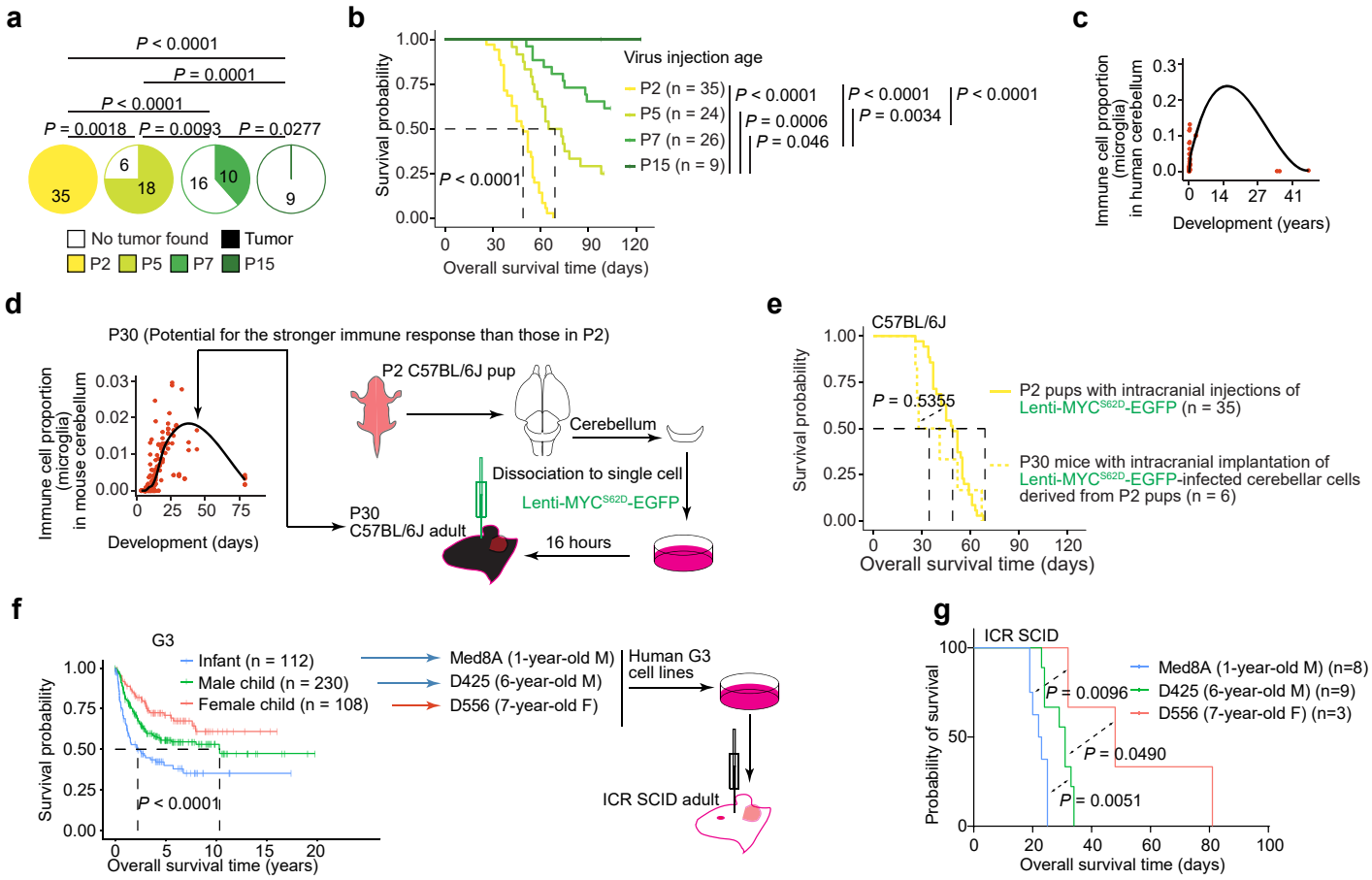

Extended Data Fig. 4 Tumor properties based on developmental origins. a, Pie charts showing incidence of tumor originated from different NPC developmental stages in pLenti-MYC^{S62D}-induced G3-like mouse models. **b**, Kaplan-Meier survival curves of tumors in **a**. **c**, Cerebellar immune cell proportions in human scRNA-seq data across development. **d**, Schematic diagram of P2 cerebellar NPC originated tumor cells transplantation into P30 C57BL/6J mice. **e**, Kaplan-Meier survival curve of mouse tumors in recipient mice with different ages. **f**, Kaplan-Meier survival curve of G3 MB patients stratified by sex and age groups (left). Schematic diagram showing orthotopic xenograft models derived from human G3 cell lines, which were originated from patients with different ages and sexes (right). **g**, Kaplan-Meier survival curve of the 3 orthotopic xenograft models in **f**. Each dot represents a merged scRNA-seq sample (**c, d**). *n* denotes the number of mouse (**b, e, g**) or human (**f**) samples. *P* values were calculated using chi-square test (**a**) or log-rank test (**b, e, f, g**).

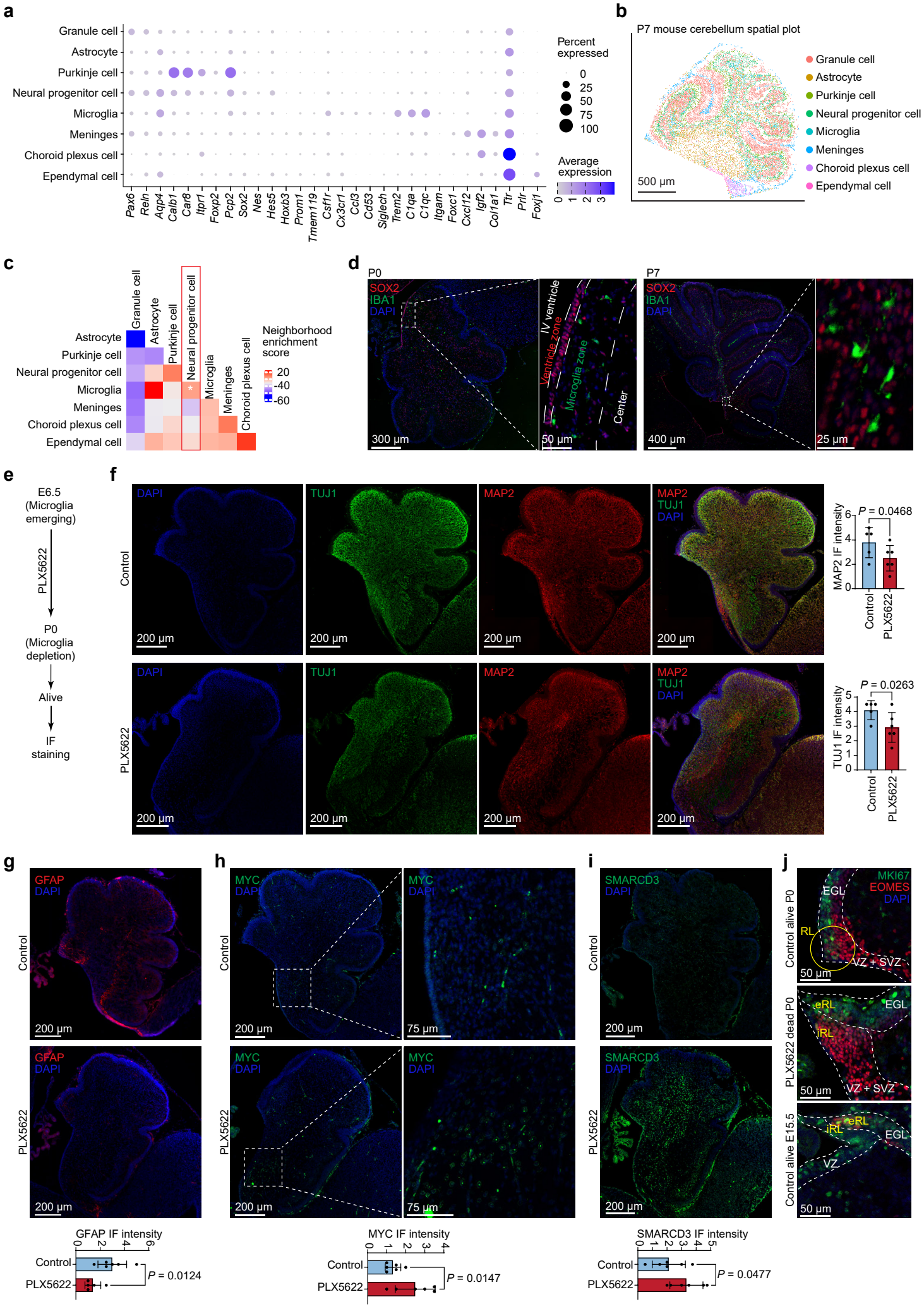
a
Granule cell
Astrocyte
Purkinje cell
Neural progenitor cell
Microglia
Meninges
Choroid plexus cell
Ependymal cell
Pax6 Reln Aqp4 Calb1 Car8 Itpr1 Foxp2 Pcp2 Sox2 Nes Hes5 Hoxb3 Prom1 Tmem119 Csf1r Cx3cr1 Ccl3 Cd53 Siglech Trem2 C1qa C1qc Itgam Foxc1 Cxcl12 Igf2 Col1a1 Ttr Prlr Foxj1
Percent expressed
0
25
50
75
100
Average expression
0 1 2 3
b
P7 mouse cerebellum spatial plot
Granule cell
Astrocyte
Purkinje cell
Neural progenitor cell
Microglia
Meninges
Choroid plexus cell
Ependymal cell
500 μm
c
Granule cell
Astrocyte
Purkinje cell
Neural progenitor cell
Microglia
Meninges
Choroid plexus cell
Ependymal cell
Neighborhood enrichment score
20
-40
-60
d
P0
SOX2
IBA1
DAPI
IV ventricle
Ventricle zone
Microglia zone
Center
300 μm
50 μm
P7
SOX2
IBA1
DAPI
400 μm
25 μm
e
E6.5 (Microglia emerging)
PLX5622
P0 (Microglia depletion)
Alive
IF staining
f
Control
PLX5622
DAPI
TUJ1
MAP2
MAP2 TUJ1 DAPI
200 μm
MAP2 IF intensity
P = 0.0468
Control
PLX5622
TUJ1 IF intensity
P = 0.0263
Control
PLX5622
g
Control
PLX5622
GFAP
DAPI
200 μm
GFAP IF intensity
Control
PLX5622
P = 0.0124
h
Control
PLX5622
MYC
DAPI
200 μm
75 μm
MYC IF intensity
Control
PLX5622
P = 0.0147
i
Control
PLX5622
SMARCD3
DAPI
200 μm
SMARCD3 IF intensity
Control
PLX5622
P = 0.0477
j
Control alive P0
PLX5622 dead P0
Control alive E15.5
MKI67
EOMES
DAPI
EGL
RL
VZ + SVZ
eRL
iRL
VZ
50 μm

Extended Data Fig. 5 Microglia promote NPC differentiation. a, Dot plot of marker gene expression in the cell types from P7 mouse cerebellum spatial transcriptome data. **b**, Spatial transcriptome map of the P7 cerebellum. **c**, Neighborhood enrichment scores indicating physical proximity between cell types based on the P7 mouse cerebellum spatial transcriptome data. **d**, IF images of microglia and NPCs in P0 and P7 mouse cerebella. **e**, Schematic of PLX5622 treatment and following cerebellar IF staining. **f–i**, IF images and quantifications of indicated marker gene expression in control *vs.* PLX5622-treated mice. **j**, IF images of the rhombic lip development across ages with/without PLX5622 treatment. Each dot represents a bin (**b**) or one biologically independent sample (**f–i**). Data are presented as the mean ± s.d. (**f–i**). *P* values were calculated using one-tailed unpaired *t*-test (**f–i**). VZ, ventricle zone; EGL, external granule layer; RL, rhombic lip; iRL, interior surface of rhombic lip; eRL, exterior surface of rhombic lip.

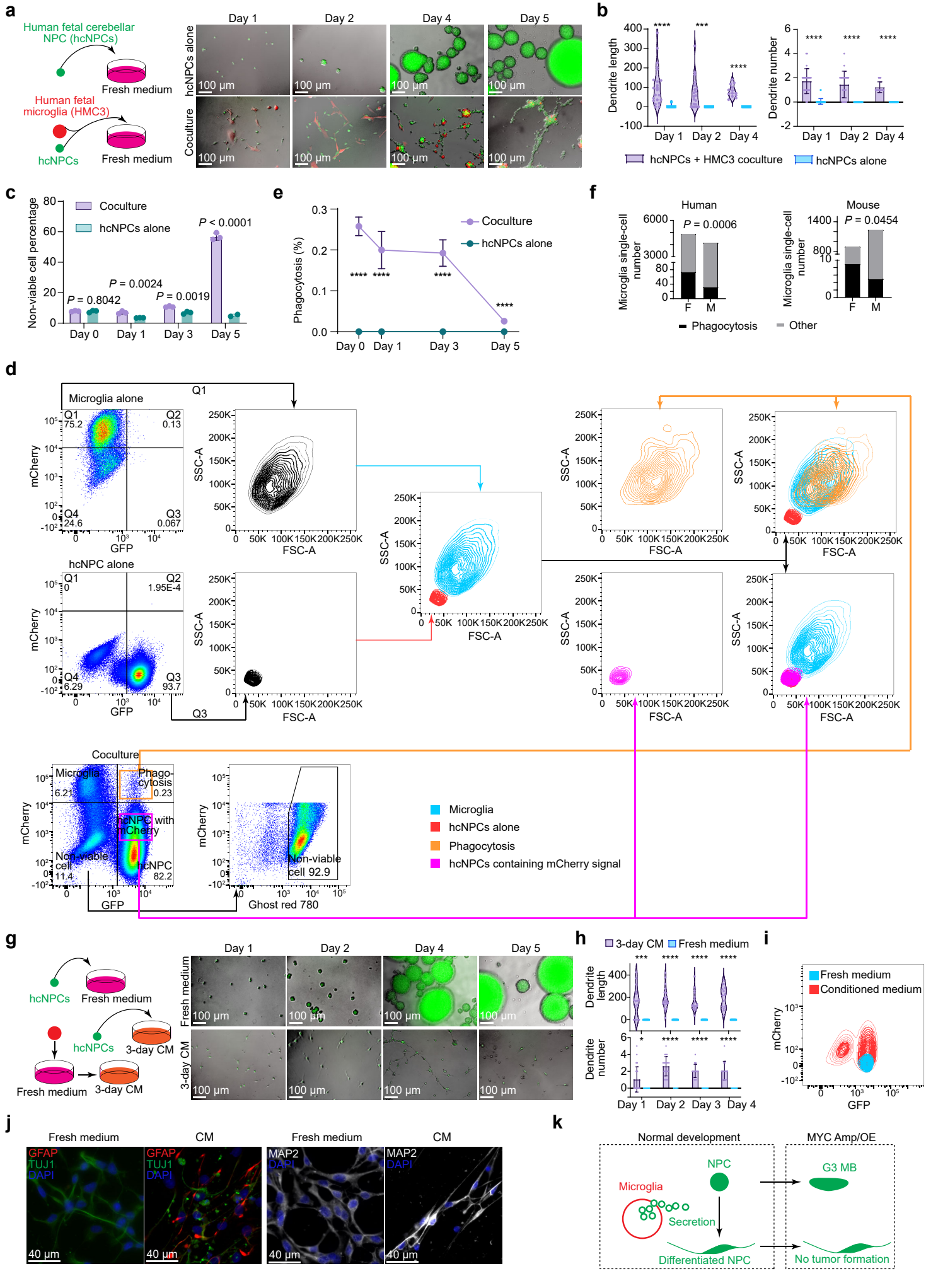
a
Human fetal cerebellar NPC (hcNPCs)
Fresh medium
Human fetal microglia (HMC3)
hcNPCs
Fresh medium
Day 1
Day 2
Day 4
Day 5
hcNPCs alone
Coculture
100 μm
b
Dendrite length
Dendrite number
Day 1
Day 2
Day 4
hcNPCs + HMC3 coculture
hcNPCs alone
c
Non-viable cell percentage
Coculture
hcNPCs alone
P = 0.8042
P = 0.0024
P = 0.0019
P < 0.0001
Day 0
Day 1
Day 3
Day 5
e
Phagocytosis (%)
Coculture
hcNPCs alone
f
Human
Mouse
Microglia single-cell number
P = 0.0006
P = 0.0454
F
M
Phagocytosis
Other
d
Microglia alone
hcNPC alone
Coculture
Q1
Q2
Q3
Q4
mCherry
GFP
SSC-A
FSC-A
Ghost red 780
Microglia
Phago-cytosis
hcNPC with mCherry
Non-viable cell
hcNPC
Microglia
hcNPCs alone
Phagocytosis
hcNPCs containing mCherry signal
g
hcNPCs
Fresh medium
3-day CM
Fresh medium
Day 1
Day 2
Day 4
Day 5
h
3-day CM
Fresh medium
Dendrite length
Dendrite number
i
Fresh medium
Conditioned medium
mCherry
GFP
j
Fresh medium
CM
GFAP
TUJ1
MAP2
DAPI
40 μm
k
Normal development
MYC Amp/OE
NPC
Microglia
Secretion
Differentiated NPC
G3 MB
No tumor formation

Extended Data Fig. 6 Microglial secretions promote NPC differentiation. a, Schematic diagrams and bright-field/fluorescence images of treated cells. **b**, Violin plots of dendrite length (left) and boxplots of dendrite number (right) for hcNPCs. **c**, Boxplots of non-viable cell percentages in hcNPCs. **d**, Flow cytometry gating for phagocytosis analysis to distinguish phagocytosis cells and hcNPCs with mCherry by cell size and granularity. **e**, Phagocytosis percentage in hcNPCs. **f**, Bar graphs showing the number of NPC-phagocytosis microglia in human and mouse cerebellum. **g**, Schematic and bright-field/fluorescence images of hcNPCs in different media. **h**, Violin plots of dendrite length and boxplots of dendrite number of the cultured hcNPCs. **i**, Flow cytometry analysis of the microglial (mCherry) signal of hcNPCs cultured in different conditioned media. **j**, IF images of the indicated marker gene expression in hcNPCs cultured in fresh *vs.* conditioned medium. **k**, Model of microglial regulation of NPC differentiation and tumor suppression. Each dot represents one hcNPC (**b, h**) or one biologically independent sample (**c**). Data are presented as mean ± s.d. (**b, c, e, h**). *P* values were calculated using two-tailed unpaired *t*-test (**b, c, e, h**) or chi-square test (**f**). ****$P < 0.0001$.

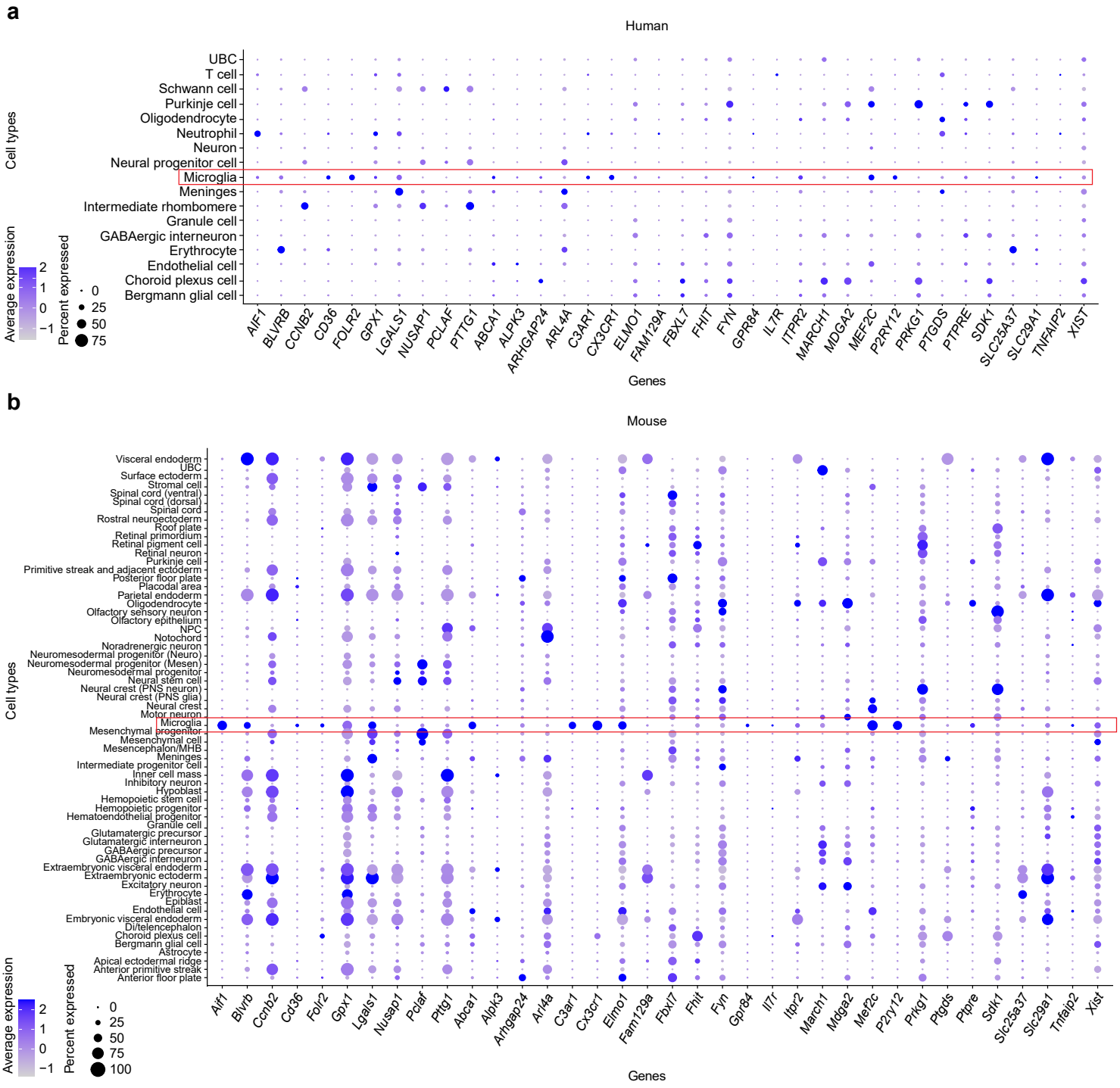

Extended Data Fig. 7 Sex-specific DEGs indicate microglial effects on NPC differentiation. a–b, Dot plots of sex-specific DEG expression per cell type in human (**a**) and mouse (**b**). **c–d**, GO enrichment for female- (**c**) and male-biased (**d**) DEGs in microglia. *P* values were calculated using two-tailed Benjamini-Hochberg corrected multiple Fisher test (**c, d**).

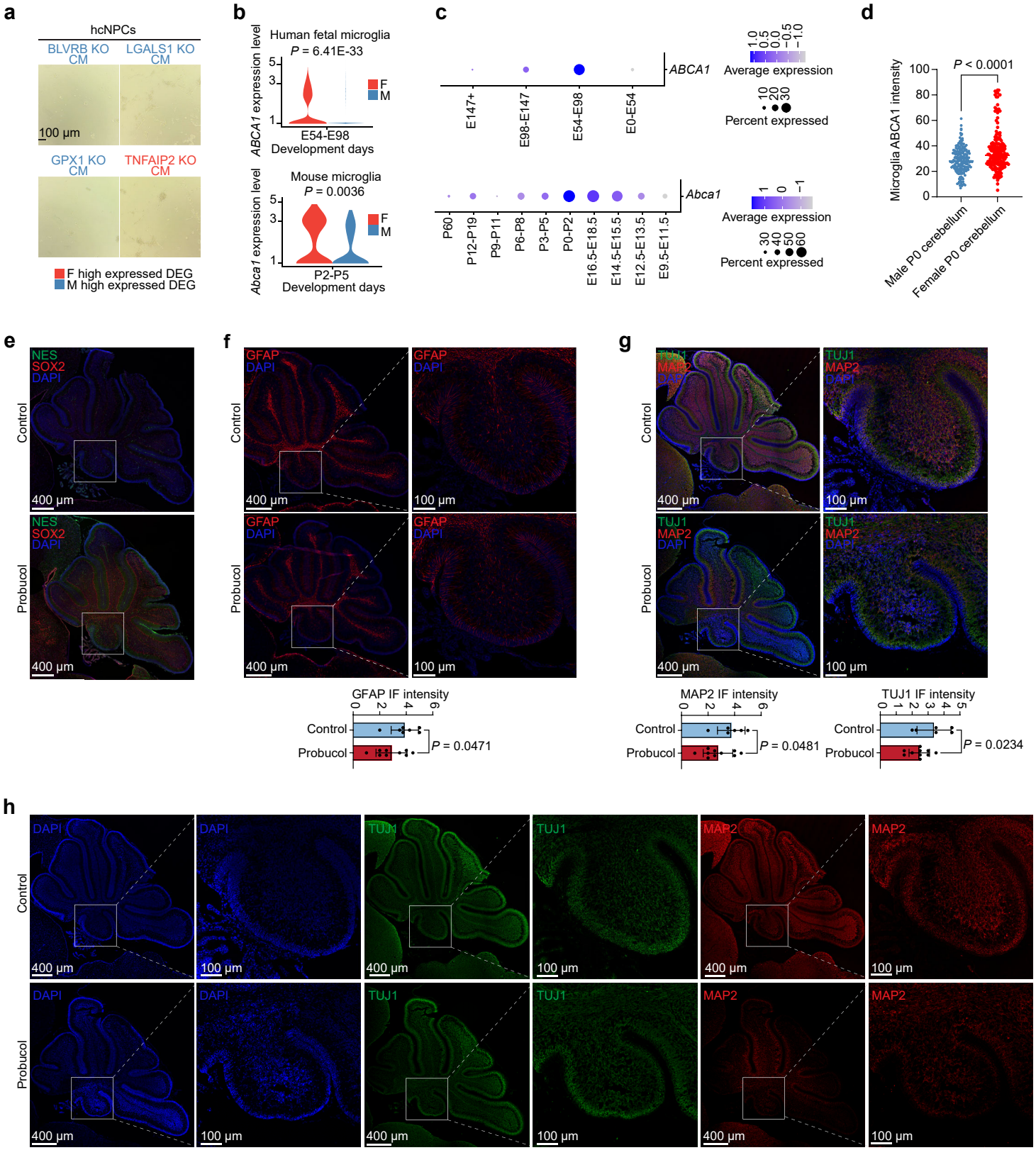

Extended Data Fig. 8 Sex differences of ABCA1 expression in microglia regulate sexual dimorphism of NPC differentiation. a, Bright-field image of hcNPCs cultured in conditioned media from genetically engineered microglia with the indicated gene deletion. **b–c**, Violin plots and dot plots of ABCA1 expression levels in cerebellar microglia during development in human and mouse. **d**, Quantification of ABCA1 IF intensity in male *vs.* female microglia from P0 C57BL/6J mice. **e–h**, IF images and quantifications of indicated marker gene expression in control *vs.* probucol-treated mice. The white line boxed regions correspond to areas in **Fig. 3d** (**e**) or nearby magnified regions (**f, g, h**). Each dot represents one cell (**d**) or one biologically independent sample (**f, g**). Data are presented as the mean ± s.d. (**f, g**). *P* values were calculated using non-parametric Wilcoxon rank sum test (**b**) or one-tailed unpaired *t*-test (**d, f, g**).

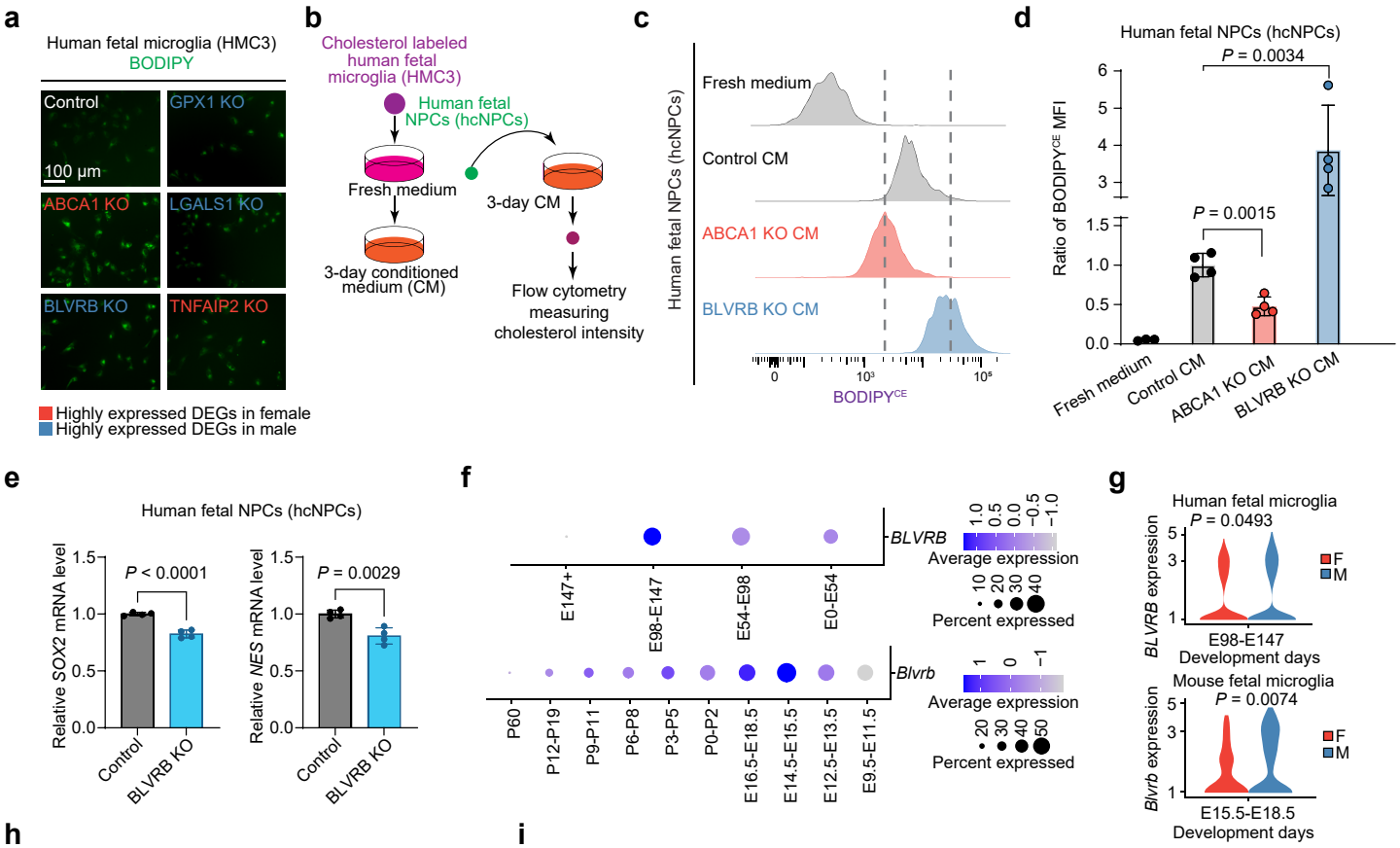

Extended Data Fig. 9 Sex differences of BLVRB-Bilirubin activation in microglia regulate NPC differentiation. a, Fluorescence images of BODIPY staining in microglia with indicated gene KO. **b**, Schematic of the procedure of cholesterol transfer from microglia to hcNPCs. **c–d**, MFI and BODIPY^{CE} quantification in hcNPCs cultured in the indicated conditioned media. **e**, RT-qPCR analysis of SOX2 and NES in hcNPCs cultured in WT *vs.* BLVRB KO microglia-conditioned media. **f–g**, Dot and violin plots of BLVRB expression levels in cerebellar microglia during development in human and mouse. **h–i**, IF images of hcNPCs cultured in the conditioned media from DMSO- *vs.* bilirubin-treated microglia. Each dot represents one biologically independent sample (**d, e**). Data are presented as the mean ± s.d. (**d, e**). *P* values were calculated using two-tailed unpaired *t*-test (**d, e**) or non-parametric Wilcoxon rank sum test (**g**).

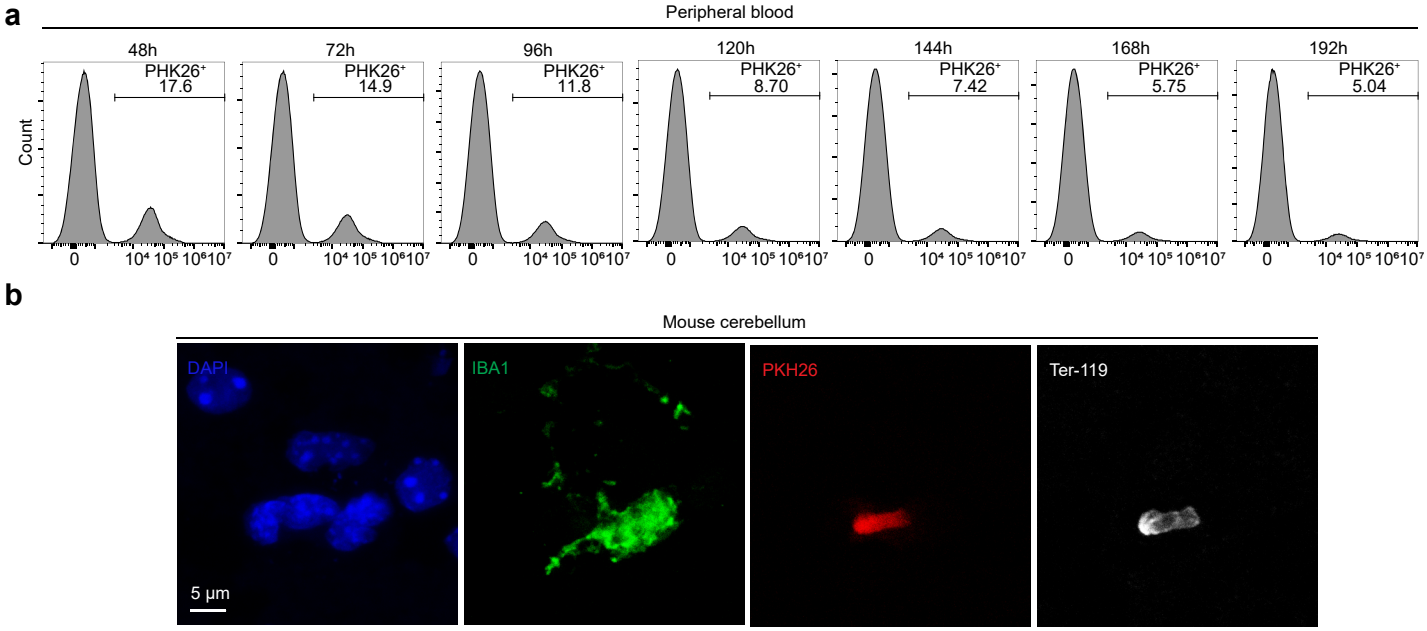

Extended Data Fig. 10 Erythrophagocytosis in mouse cerebellar microglia. a, Flow cytometry analysis of peripheral blood post injection of PHK26⁺ RBCs. **b**, IF images of erythrophagocytosis in P7 mouse cerebellum (63×).

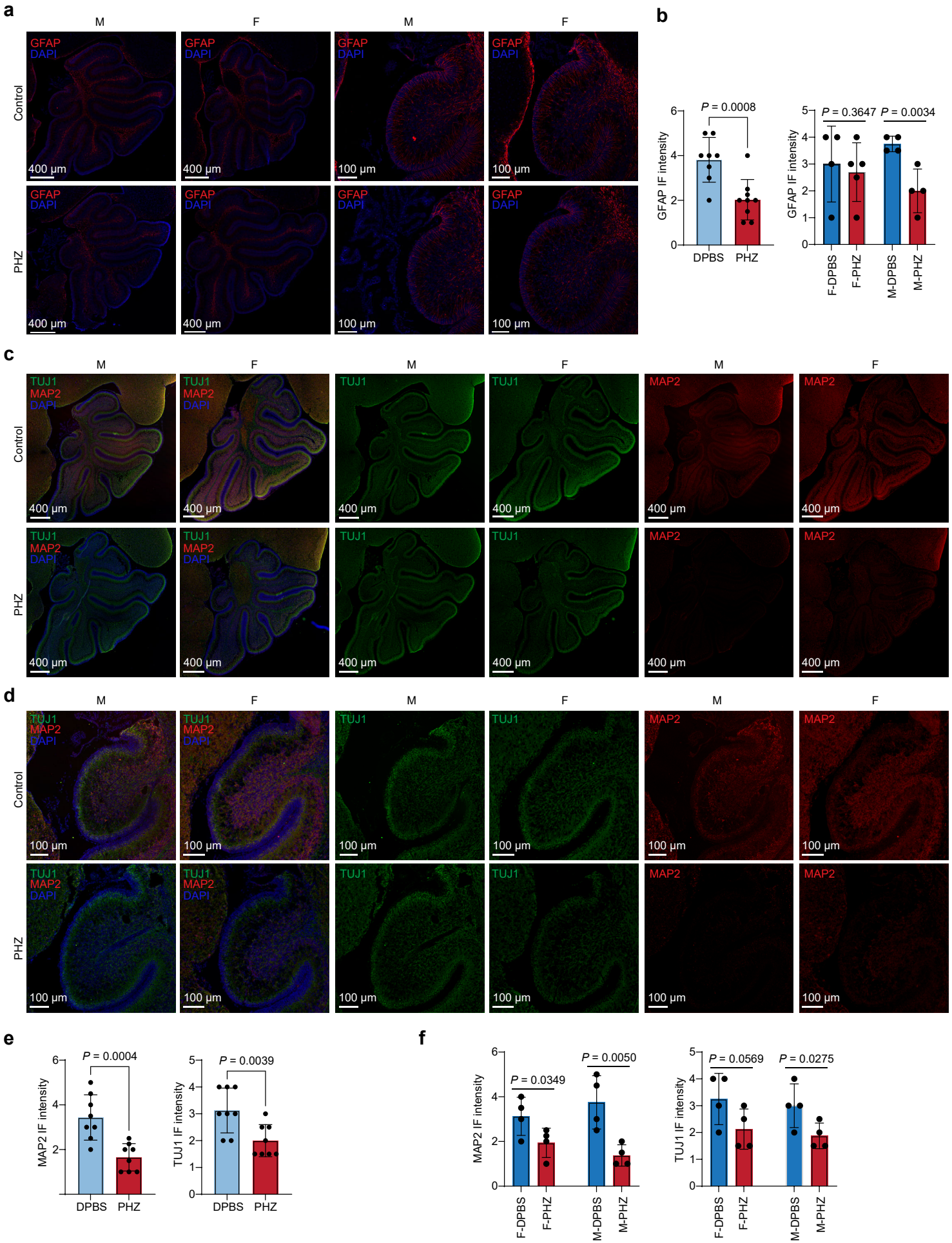

Extended Data Fig. 11 PHZ-induced microglial erythrophagocytosis inhibits NPC differentiation. a–b, IF images and quantification of GFAP expression in the cerebellum of P7 mice treated with DPBS *vs.* PHZ. **c–f**, IF images and quantification of TUJ1 and MAP2 expression in the cerebellum of P7 mice treated with DPBS *vs.* PHZ. Each dot represents one mouse (**b, e, f**). Data are shown as mean ± s.d. (**b, e, f**). *P* values were calculated using one-tailed unpaired *t*-test (**b, e, f**).

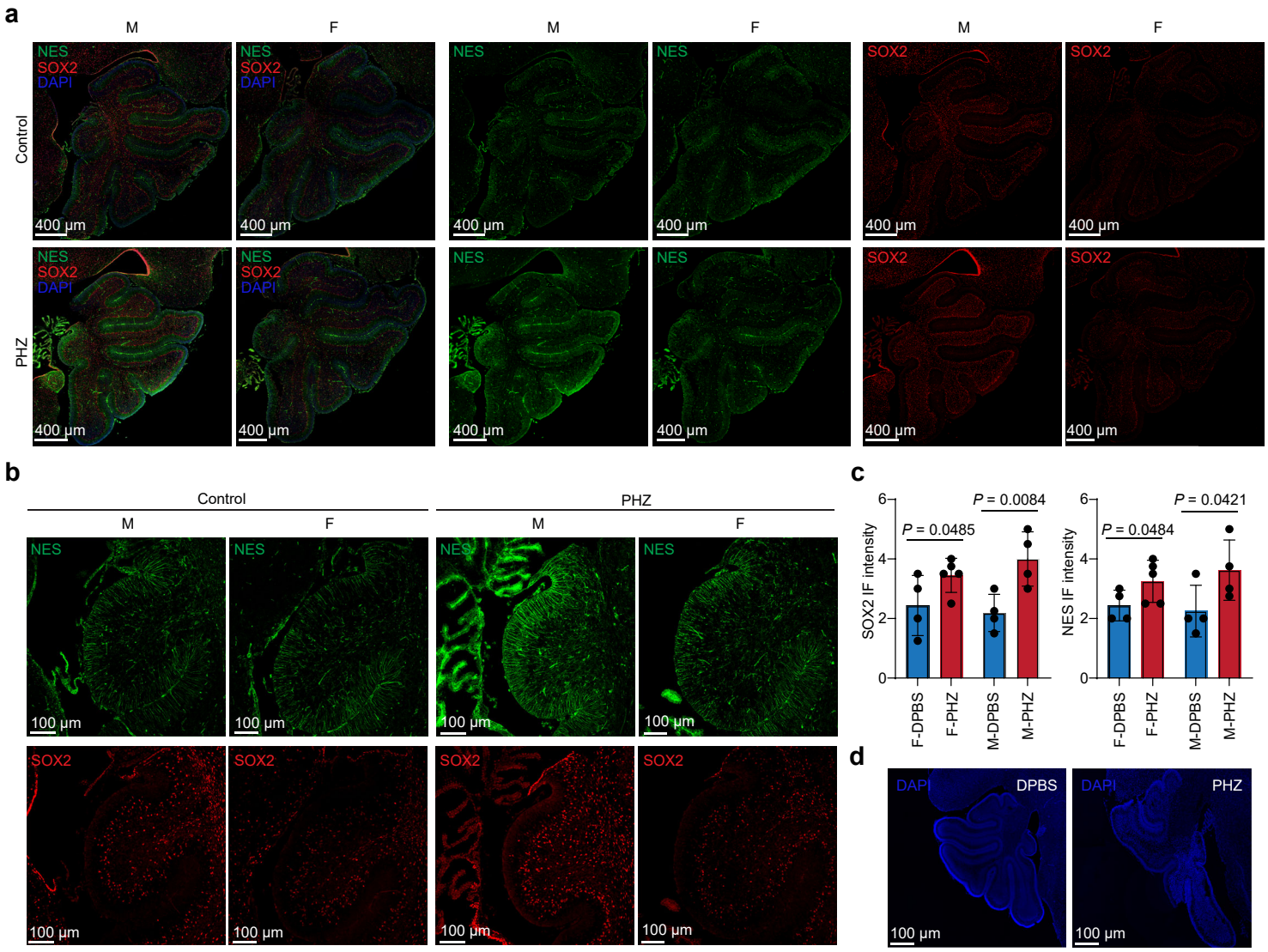

Extended Data Fig. 12 PHZ-induced microglial erythrophagocytosis inhibits NPC differentiation and cerebellar maturation. a–c, IF images and quantification of SOX2 and Nestin expression in the cerebellum of P7 mice treated with DPBS *vs.* PHZ. **d**, Morphological comparison of cerebella in mice treated with DPBS *vs.* PHZ. Each dot represents one mouse (**c**). Data are shown as mean ± s.d. (**c**). *P* values were calculated using one-tailed unpaired *t*-test (**c**).

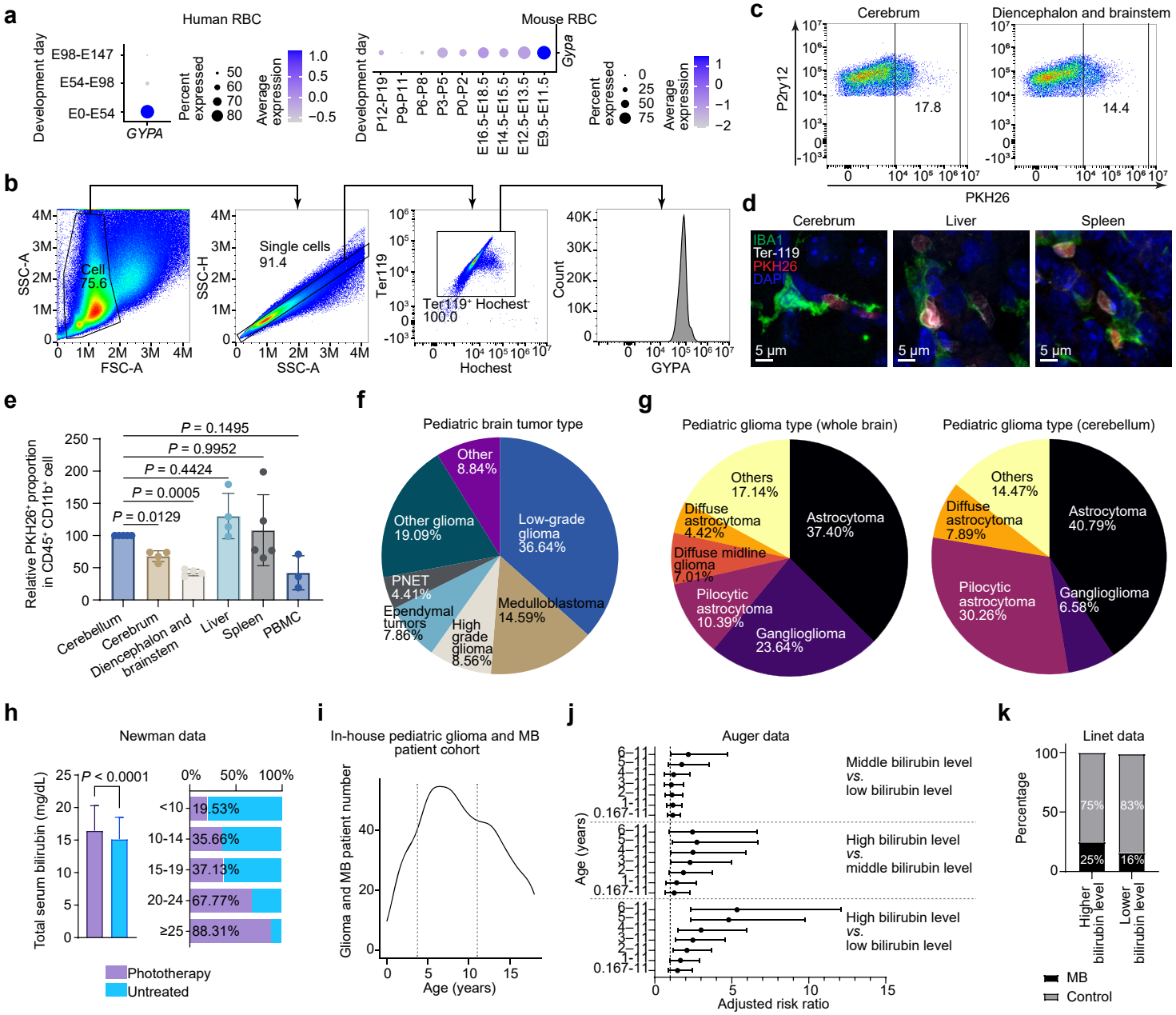

Extended Data Fig. 13 Sex differences in erythrocytic GYPA expression, bilirubin levels, and pediatric brain tumorigenesis. a, Dot plots showing GYPA expression levels in erythrocytes during development in human and mouse. **b**, Flow cytometry gating strategies of erythrocytes. **c**, Flow cytometry analysis of erythrophagocytosis of CD45$^+$ CD11b$^+$ P2ry12$^+$ cells from different mouse brain regions. **d**, IF images of erythrophagocytosis in P7 mouse cerebrum, liver and spleen (63x). **e**, Quantification of erythrophagocytosis ability of CD45$^+$ CD11b$^+$ cells from different mouse brain regions and organs. **f**, Pie chart showing the distribution of pediatric brain tumor types. **g**, Pie charts showing the distribution of pediatric glioma types in our in-house cohort. **h**, Histogram and bar graphs of total serum bilirubin levels corresponding to patient groups with and without phototherapy. **i**, The age distribution of pediatric glioma and MB incidence in our in-house brain tumor cohort. **j**, Forest plot showing the risk ratio of pediatric brain tumors diagnosed at different ages in relation to abnormal bilirubin levels at birth. **k**, Bar graph comparing the MB incidence between patients born with high *vs.* low bilirubin levels. Each dot represents one biologically independent sample (**e**). Data are presented as the mean ± s.d. (**e, h**) or the mean ± 95% confidence interval (**j**). *P* values were calculated using one-way ANOVA (**e**) or two-tailed unpaired *t*-test (**h**).

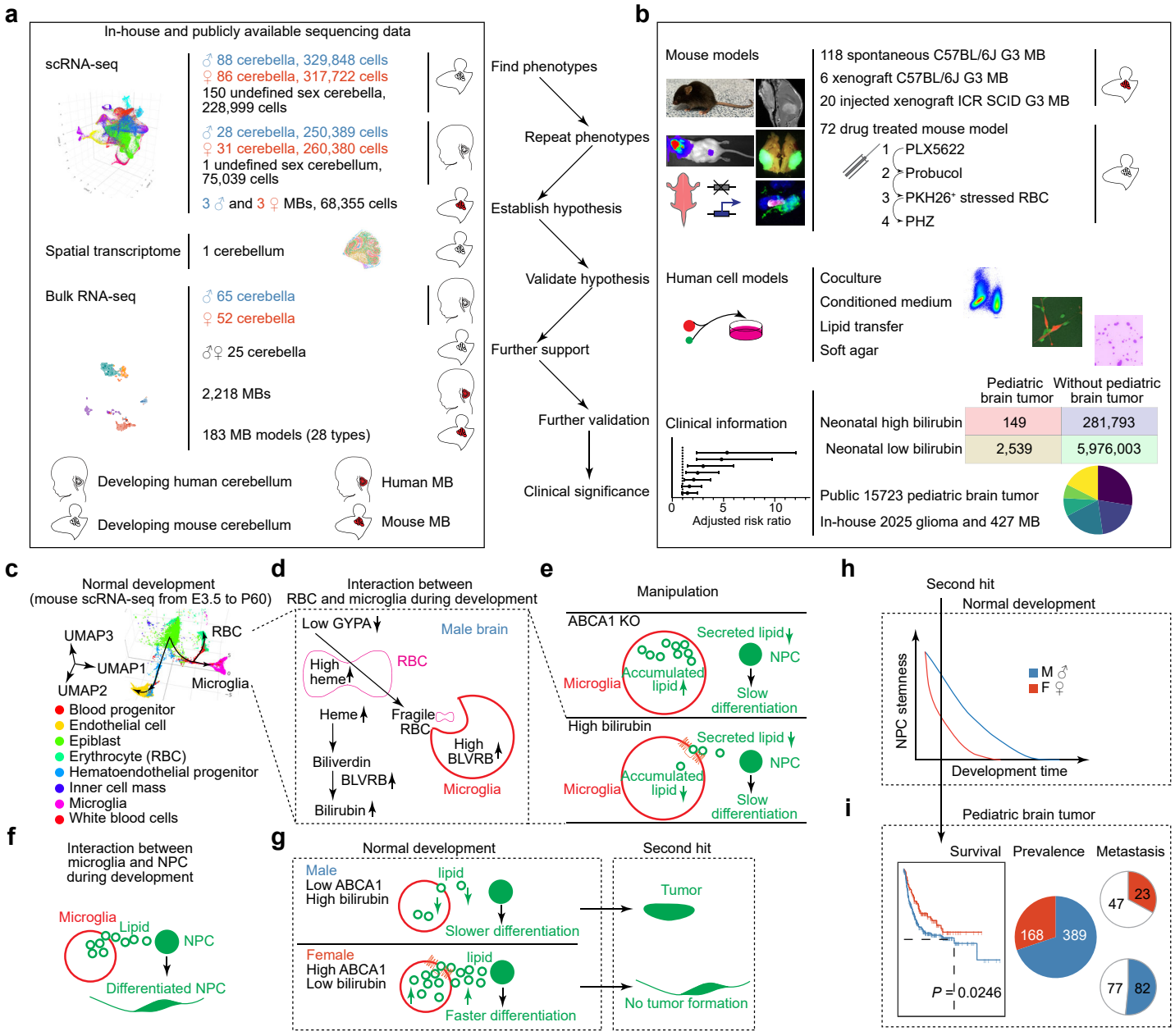

Extended Data Fig. 14 Erythrocyte-microglia-NPC interaction mediates sex differences in pediatric brain tumorigenesis through ABCA1-BLVRB/bilirubin regulated lipid secretion. a, Schematic summary of molecular datasets linking cerebellar development and MB with sex differences. **b**, Overview of *in vivo*, *in vitro*, and clinical experiments validating mechanisms underlying sex differences in pediatric brain tumor. **c**, UMAP visualization of microglia and RBC development in mice from E3.5 to P60 based on scRNA-seq data. **d**, Schematic representation of microglial bilirubin production in male. **e**, Illustration of manipulated microglia influencing NPC differentiation. **f**, Diagram depicting that microglia promote NPC differentiation during development. **g**, Schematic of sex differences in microglia inducing sex differences in NPC differentiation and tumorigenesis. **h**, Illustration of sex differences in NPC differentiation. **i**, Schematic of how sex differences in NPC differentiation contribute to variations in survival, prevalence and metastasis of pediatric brain tumors.